

An apodizing phase plate coronagraph for VLT/NACO

Matthew A. Kenworthy^{a,b}, Sascha P. Quanz^c, Michael R. Meyer^c, Markus E. Kasper^d, Rainer Lenzen^e, Johanan L. Codona^b, Julien H.V. Girard^f, and Philip M. Hinz^b

^aLeiden Observatory, Leiden University, P.O. Box 9513, 2300 RA Leiden, The Netherlands;

^bSteward Observatory, 933 N. Cherry Avenue, Tucson, AZ 85721, USA;

^cInstitut für Astronomie, ETH Zürich, Wolfgang-Pauli-Strasse 27, 8093 Zürich, Switzerland;

^dEuropean Southern Observatory, Karl-Schwarzschild-Str. 2, D-85748 Garching, Germany;

^eMax-Planck-Institut für Astronomie, Königstuhl 17, 69117 Heidelberg, Germany;

^fEuropean Southern Observatory, Casilla 19001, Santiago, Chile

ABSTRACT

We describe a coronagraphic optic for use with CONICA at the VLT that provides suppression of diffraction from 1.8 to 7 λ/D at 4.05 microns, an optimal wavelength for direct imaging of cool extrasolar planets. The optic is designed to provide 10 magnitudes of contrast at 0.2 arcseconds, over a “D” shaped region in the image plane, without the need for any focal plane occulting mask.

Keywords: coronagraph, high contrast, adaptive optics, thermal infrared

1. INTRODUCTION

Many telescopes are being used in the quest for direct imaging of extrasolar gas giant planets around nearby stars. Detecting the signal of an extrasolar planet directly is challenging due to the large contrast ratio expected between the planet and star. To date, most surveys for extrasolar planets have obtained null results constraining the frequency of young gas giants at large orbital radii (> 30 AU). However, recent notable successes^{1–6} have provided evidence for rare, yet remarkable systems that challenge our ideas of planet formation. Based on our understanding of circumstellar disks that surround young sun-like stars, as well as hints from radial velocity surveys, we expect most planet formation to occur between 3 – 30 AU.

To this end, coronagraphs are employed to minimise the scattered and diffracted flux from the host star that can obscure the signal from the exoplanet. Other techniques, such as SDI, have lower throughput since narrow band filters are utilised, and depend on the veracity of atmospheric models, requiring a methane absorption feature ($T_{eff} > 1200K$) to distinguish the planet from the host star.

Imaging in the thermal IR from 3 – 5 μm enables searches for colder planets. Consequently, surveys can concentrate on older stars that tend to be closer to the Sun, permitting searches at smaller physical separations comparable to the dimensions of our Solar System when employed to study the nearest stars. Using an APP coronagraph,⁷ broadband observations at longer wavelengths (where the planet/star contrast ratio is more favourable) such as L and M band, in combination with the AO system at the VLT, will enable exoplanet searches at small (< 0.5 arcseconds) angular separations corresponding to 3 – 30 AU around nearby candidate stars (6 – 60 pc).

As we are just on the verge of many new exoplanet detections, we believe this factor of three will yield an unanticipated number of new discoveries. In addition, this capability can be used to improve characterization of objects discovered at other wavelengths, improving constraints on the physical characteristics of planets from broader wavelength coverage. Finally, we speculate that the thermal IR will emerge as the wavelength of choice to study the formation of terrestrial planets through detection of hot protoplanet collision afterglows such as predicted from models of the formation of the Earth-Moon system.^{8–11}

The APP coronagraph has broad applicability, useful for imaging and characterization of any astronomical object with faint extended structure surrounding bright targets, including, but not limited to, extrasolar planets.

Send correspondence to M.A.K. E-mail: kenworthy@strw.leidenuniv.nl, Telephone: +31 (0)71 527 8455

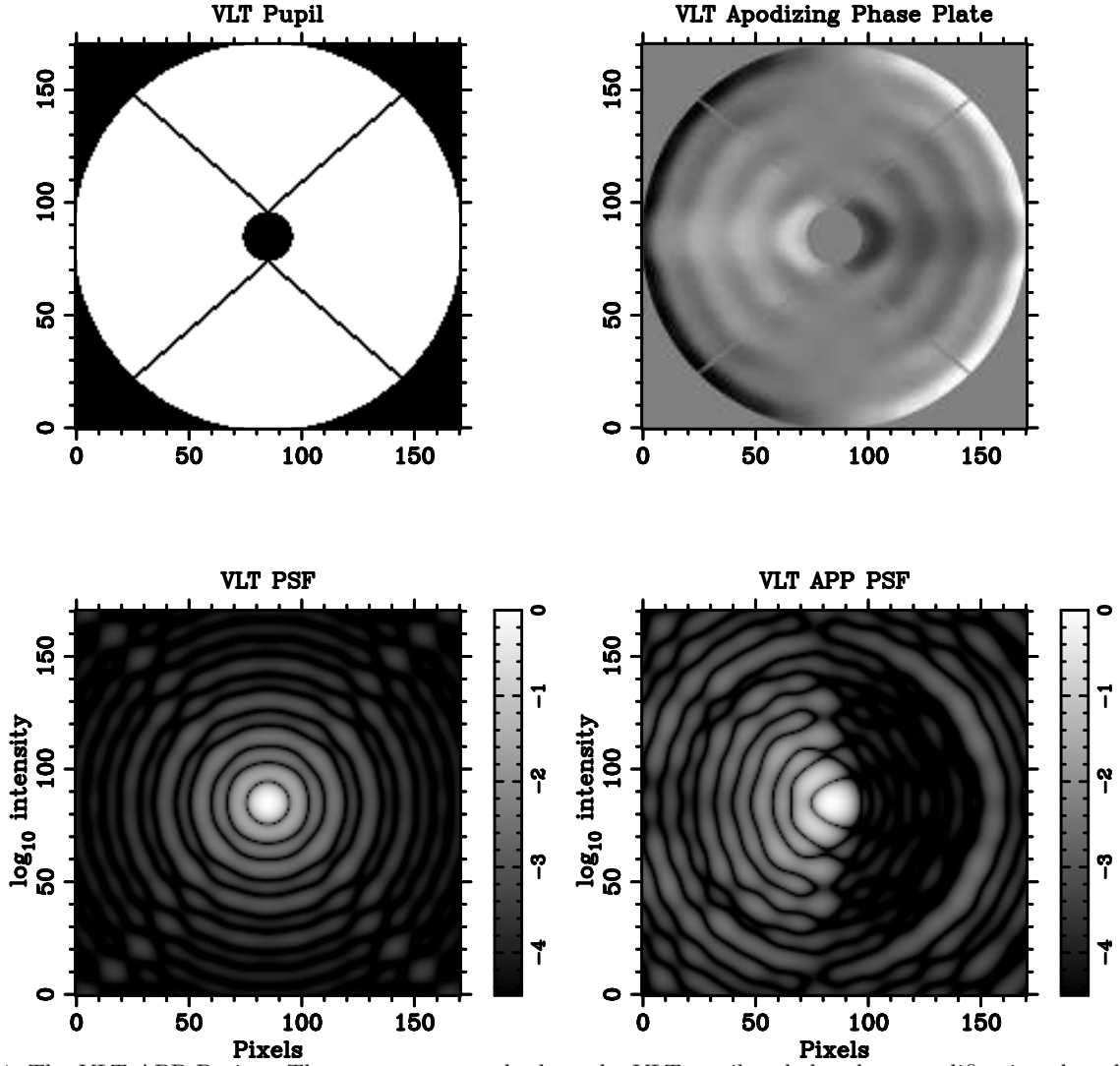


Figure 1. The VLT APP Design. The upper two panels show the VLT pupil and the phase modification that the APP optic introduces to the VLT pupil. The resultant PSFs are shown in the lower two panels, with a logarithmic intensity scale normalised to the peak flux in each case. The encircled energy flux for the APP is 59% of the unobstructed VLT PSF flux at $3 - 5\mu m$.

2. PRINCIPLE OF THE APODIZING PHASE PLATE

2.1 Overview

Like many other telescopes and imaging cameras, CONICA has a pupil filter wheel that is coincident with the location of the reimaged telescope pupil. At this point in the optical train, the pupil image is at a location where the wavefront from a distant astronomical object is nominally flat and planar. The resultant image at the science camera has the typical point spread function (PSF) of a large, adaptive optic corrected telescope. By modifying the wavefront phase at this pupil plane, this Airy ring pattern can be rearranged and diffraction rings suppressed over a 180° field of view “D” shaped region,^{7,12} see Figure 1. The reduction in Airy ring flux is shown in Figure 2 where the effect of the APP shows suppression by a factor of 10 to 50.

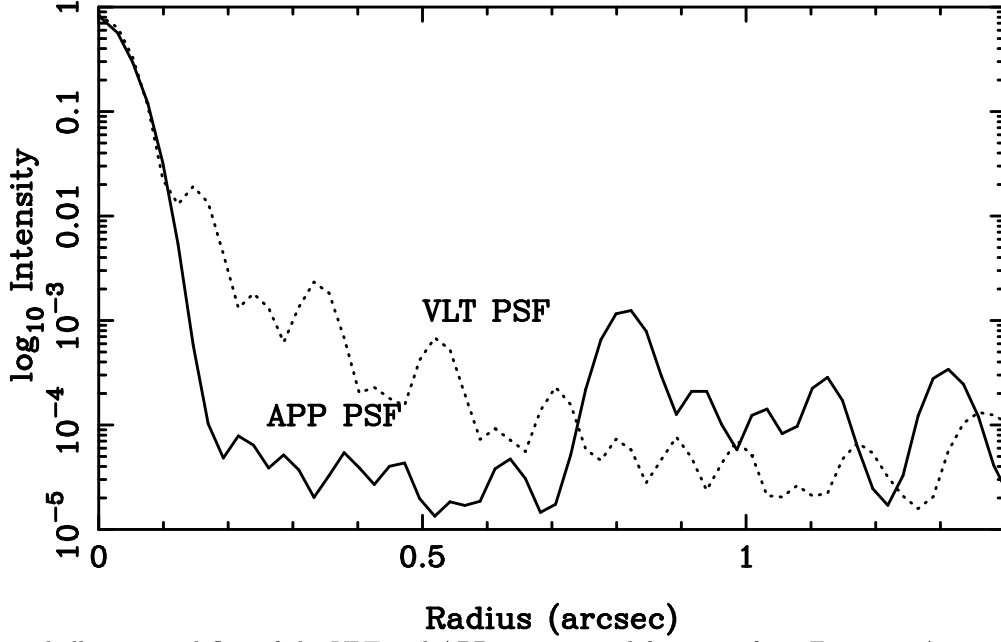


Figure 2. Azimuthally averaged flux of the VLT and APP point spread functions from Figure 1. Average over a wedge 150° centered over the dark D of the APP.

2.2 Resultant Point Spread Function (PSF) using the APP

All coronagraphs suffer from a loss of sensitivity, due to the scattering of science light through the optics. Focal plane masks block out the central star and an extended region surrounding it, resulting in a lack of close-in sensitivity and a loss of angular resolution when a Lyot stop is used in the pupil plane. Furthermore, there is a cost in the overhead used in aligning the coronagraph with the host star.

The APP is different because there is no amplitude apodization - all of the flux of the pupil is transmitted through the APP, only the phase is modified. Since we are using light from the core of the PSF to suppress diffraction over one half of the PSF, there is a reduction in the core intensity of all objects in the field of view of the camera, including the planet and host star. The degree of core flux lost is a trade-off between level of suppression, the smallest inner working angle that the suppression can go to, and the core flux.¹³ We choose an (APP/Direct Imaging) core flux ratio of 59% (see Figure 1). The integration required to get complete coverage around a host star and reach the same signal to noise as direct imaging is 4 times longer, but this is more than compensated for by the **additional sensitivity at small IWAs which are otherwise inaccessible without a coronagraph**.

2.3 Realization of the APP Coronagraph

Variations in the thickness of a Zinc Selenide substrate introduces optical path differences that correspond to variations in phase across the telescope pupil. The variation in phase, $\Delta\phi$, is related to variations in the thickness of the substrate Δx by the refractive index n of the transmitting material: $\Delta\phi = (2\pi/\lambda).\Delta x.(n - 1)$, which is an inherently chromatic process. However, the performance of the APP degrades only slowly with increasing bandwidth and the plate is used at 20% bandwidth at the MMT from $3 - 5\mu m$.

The VLT APP is manufactured in a multi-stage process. First, a blank of Zinc Selenide has a pedestal with the same dimensions to the telescope pupil machined into its surface. A gold coating is deposited over the side of the optic with the pedestal, and then the APP phase pattern is machined into the pedestal, removing the gold mask in the process. The optic is then anti-reflection coated for a central wavelength of $4.05\mu m$. The final optic is shown in Figure 3.

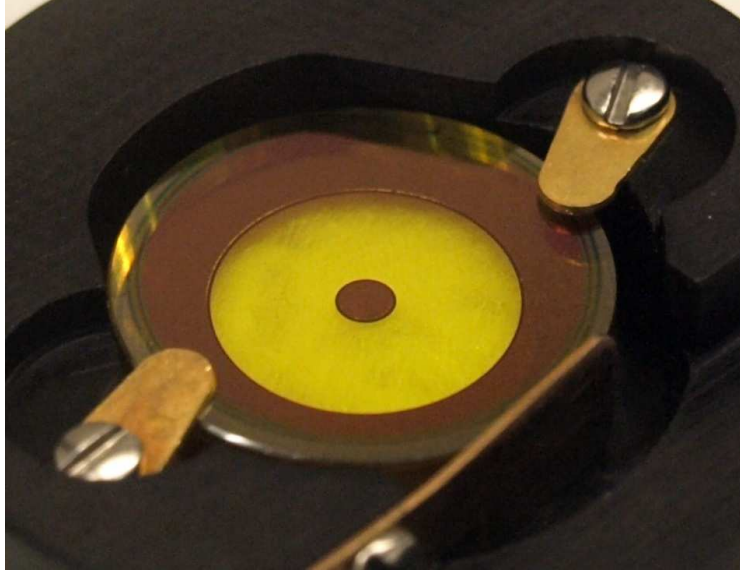


Figure 3. Photograph of VLT APP Optic mounted in holder. The light yellow area is anti-reflection coated Zinc Selenide, the darker areas are gold coated to prevent stray light from a misaligned pupil passing through the plate.

3. FIRST LIGHT PERFORMANCE AT THE VLT

We now summarize the results of the commissioning run for the APP coronagraph that was recently installed in the CONICA camera mounted at VLT UT4. The commissioning tests were carried out on April 2 and 3, 2010. The objectives were to characterize the performance of the APP so that observers can accurately plan and carry out their observations. All tests were made with the narrow band filter NB4.05 or the L' filter ($\lambda_{\text{cen}} = 3.8 \mu\text{m}$) using the L27 camera with a pixel scale of $0.027''/\text{pixel}$. The new intermediate band filter IB4.05 could not be tested with the APP due to difficulties obtaining a proper focus.

4. ALIGNMENT OF THE APP WITH THE PUPIL

In order to take full advantage of the APP capabilities it is necessary that the APP is well aligned with the pupil. As shown in Fig. 4 a misalignment between the APP and the pupil leads to imperfect suppression of the diffraction rings in the normally “clean” part of the PSF between $\sim 0.2\text{--}0.7''$. As the APP sits in the Lyot wheel there is only one remaining degree of freedom (the rotation of the wheel) that can be changed in order to achieve best possible alignment. Changing the position of the APP in the wheel in radial direction with respect to the Lyot wheel center is not possible.

The first test during the commissioning run was to ensure that the encoder position of the Lyot wheel when the APP is inserted in the light path corresponds to the best possible alignment between APP and pupil. For this purpose the bright standard star HIP39156 (K0 III, $L' = 5.1 \text{ mag}$) was observed in the NB4.05 filter (DIT = 1 s, NDIT = 30, NINT = 5)* with different encoder positions. The resulting images were compared to simulations in order to determine any possible offsets between the APP and the pupil. In total 10 different encoder positions were analyzed and the best results were obtained for an encoder position of 48595. This value was taken as the default encoder position for the rest of the commissioning run. Figure 5 shows the corresponding PSF.

5. THROUGHPUT MEASUREMENTS

The APP takes energy from the core of the PSF and redistributes it so that the diffraction pattern in one hemisphere is suppressed while it is enhanced in the other hemisphere. As a result, the flux in the PSF core is

*DIT = “Detector Integration Time”, NDIT = Number of coadds with same DIT in a single file; NINT = the total number of dither positions for which exposures of $\text{DIT} \times \text{NDIT}$ s were obtained.

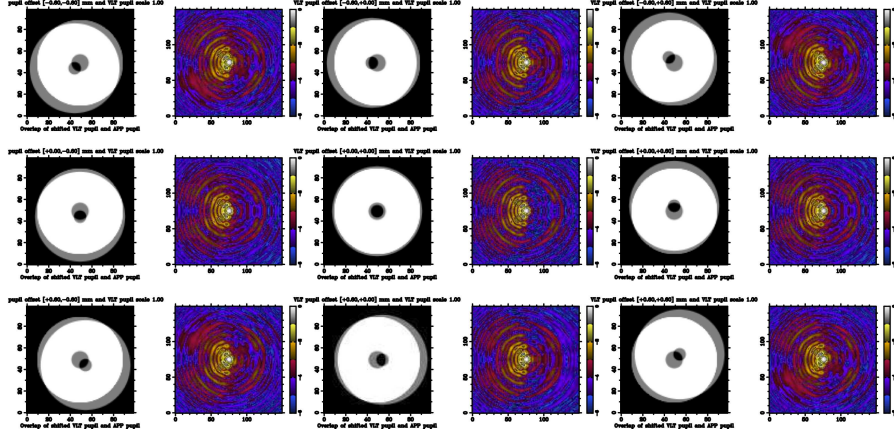


Figure 4. Simulations showing the effect of APP-pupil misalignment on the predicted PSF. The center image pair shows a perfectly aligned APP (white) with the VLT pupil (grey) and an almost perfectly clean hemisphere on the righthand side of the APP PSF where the diffraction pattern is effectively suppressed. The other image pairs show the result from offsets of $60\ \mu\text{m}$ between the APP and the VLT pupil in positive and negative x and y direction and combinations thereof. The effectiveness of the diffraction ring suppression is worse in all cases.

lower compared to non-APP observations. This flux reduction is quantified below in order to help the planning of APP observations.

5.1 Throughput in NB4.05 filter

5.1.1 Observational setup

For this test the bright standard star HIP52804 (K0 III, $L' = 4.3$ mag) was used. First, a set of exposures was taken without the APP, then an equivalent set with the APP. The time lag between the exposures without and with the APP was roughly 10 minutes. The exposures had $\text{DIT} = 0.35$ s, $\text{NDIT} = 30$, and $\text{NINT} = 5$ and were repeated three times yielding in total 15 individual images each having ~ 10.5 s integration time. The airmass was < 1.1 and the DIMM seeing was $\sim 0.9''$ and $\sim 0.85''$ without and with the APP, respectively.

5.1.2 Basic data reduction steps

Bad pixels deviating by $3\text{-}\sigma$ from the mean of a surrounding 5 pixel box were replaced by the mean of the neighboring pixels. Dark current and sky background were eliminated by subtracting two consecutive images taken at different dither positions from each other. The remaining background level was always close to zero.

5.1.3 Throughput analysis

To determine the throughput of the APP, the count rate in the inner pixels of the PSF in each individual image was computed using the IDL routine `ATV.pro`. Two different aperture sizes were used (2 pixel radius and 5 pixel radius). Table 1 summarizes the results. The count rate is the mean of the 15 individual images and the error is the corresponding standard deviation of the mean value. The throughput is simply the ratio of the count rates with and without the APP. It shows that for the NB4.05 filter the throughput in the PSF core is 59% and 63% for an aperture with a radius of 2 and 5 pixels, respectively. This is in very good agreement with theoretical predictions that estimated a value of $\sim 56\%$ in the innermost regions of the PSF core.

5.2 Throughput in L' filter

For the L' filter ($\lambda_{\text{cen}} = 3.8\ \mu\text{m}$) the bright standard star HIP61460 (F2 V, $L' = 6.2$ mag) was used. Again, first a set of exposures was taken without the APP, then an equivalent set with the APP. The time lag between the exposures without and with the APP was roughly 10 minutes. The exposures had $\text{DIT} = 0.175$ s, $\text{NDIT} = 30$, and $\text{NINT} = 5$ and were repeated three times yielding in total 15 images each having ~ 5.25 s integration

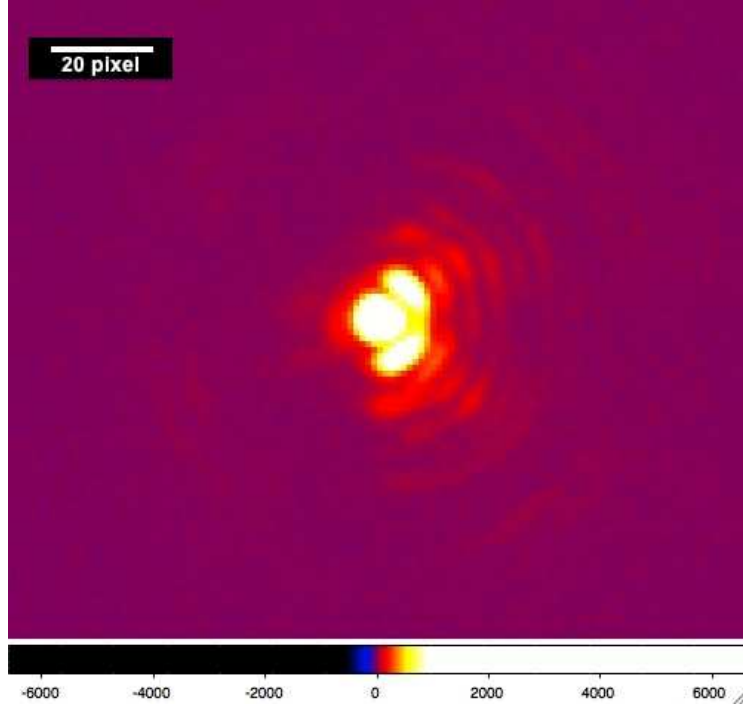


Figure 5. NACO/APP PSF after the alignment test. The “clean” part of the PSF is seen in the left hemisphere where the diffraction pattern is suppressed compared to the non-corrected hemisphere. The image is a single 30 sec exposure (DIT = 1 s, NDIIT = 30) of HIP39156 in the NB4.05 filter. Dark current and sky background were eliminated by subtracting the consecutive image of the dither pattern from this exposure.

Table 1. Throughput measurements for the VLT APP as measured in April 2010.

	2 pixel	5 pixel
NB 4.05 filter	0.59 ± 0.04	0.63 ± 0.03
L' filter	0.55 ± 0.04	0.61 ± 0.03

time. The airmass was <1.1 and the DIMM seeing was $\sim 0.6\text{--}0.8''$ for all exposures. The basic data reduction and throughput analysis was the same as described in the previous sections.

Table 1 summarizes the results for the L' filter. The throughput in the PSF core is roughly 55%, again in agreement with the models.

6. CONTRAST CURVE MEASUREMENTS

6.1 Contrast curve in the L' filter

6.1.1 Observational setup

HIP61460 (F2 V, $L' = 6.2$ mag) was used for the test in the L' filter ($\lambda_{\text{cen}} = 3.8 \mu\text{m}$). The observations were done in pupil tracking mode with DIT = 0.175 s, NDIIT = 30, and NINT = 5 yielding 5 images at different dither positions. To obtain in total roughly 30 minutes on source integration time this observing template was repeated 70 times yielding in total 350 individual image/files. All images were in the linear detector regime ($\sim \frac{1}{3}$ Full Well). The DIMM seeing varied typically between $\sim 0.7\text{--}0.8''$ and the airmass was <1.1 .

6.1.2 Basic data reduction steps

Bad pixels deviating by $3\text{-}\sigma$ from the mean of a surrounding 5 pixel box were replaced by the mean of the neighboring pixels. Dark current and sky background were eliminated by subtracting two consecutive images from each other. The remaining background level was always close to zero. Afterwards, all images were aligned with an accuracy of 0.1 pixel using cross-correlation.

6.1.3 Computation of contrast curve and results

All images were stacked together and a “MEAN image” and a “RMS image” were created by computing the mean and the r.m.s. of each pixel in the stack. Then, the mean flux per pixel in the core of the PSF was computed in an aperture with a 5 pixel radius.

$$\bar{f}_{core} = \frac{\sum_{i=1}^n f_i}{n} \quad (1)$$

with f_i being the flux in the individual pixels and n being the number of pixel considered ($5^2 \cdot \pi \approx 78$ in our case). The “RMS image” was divided by the square root of the number of individual images in the stack, i.e., 350. The resulting “One sigma image” ($\text{Im}_{1\sigma}$) contains the one sigma noise for a single pixel planet. To compute the contrast as a function of radius, we have to take into account that the flux of a potential companion will be distributed across several pixels and we have to use the same 5 pixel aperture that we used for the PSF core, i.e., n pixel. This will increase the signal to noise by a factor \sqrt{n} . Thus, the “5- σ Contrast image” in units of magnitudes can be computed using

$$\text{Im}_{5\sigma} = -2.5 \cdot \log \left(\frac{5 \cdot \text{Im}_{1\sigma}}{\sqrt{n}} \frac{1}{\bar{f}_{core}} \right) \quad (2)$$

In this image each pixel contains an estimate of the delta magnitude of a 5- σ point source detection with respect to the central core PSF. Fig. 6 shows the corresponding contrast curve for HIP61460. The contrast curve was derived in the “clean” hemisphere of the PSF in a wedge with a 160° opening angle. The values plotted in Fig. 6 correspond to the mean value of 4-pixel wide semi-annuli in this wedge for a given radial distance.

6.2 Discussion of the contrast curve

The contrast curve shown in Figures 6 show that the APP is working as expected and approximately as predicted from simulations. The steep drop of the curve at very small inner working angles demonstrates the specific strength of the APP, namely enhancing the achievable contrast close to the central star compared to non-APP images.

Although we took contrast curve data for the APP in the NB4.05 and IB4.05 filters, we did not get enough data to explore the contrast limits of the phase plate. We reach the background limit for the L' filter at $0.5''$. The APP is specifically designed to achieve the best performance at $4.05\mu\text{m}$ with the NB4.05 filter and the new IB4.05 filter. However, our tests have demonstrated that the APP performs very well with the L' filter as well, and since the bandwidth for the NB and IB filters are narrower than that for the L' filter, we expect that the performance will be at least comparable to or better than the L' filter contrast curve.

7. CONCLUSIONS

In general, the APP is expected to work best (in terms of contrast) around $4\mu\text{m}$ in combination with the NB4.05 and with the IB4.05 filter. Our results with the L' filter confirm that the APP is working well, and expected to obtain higher contrasts at narrower bandwidths.

Observing with the APP should not increase the overhead that has to be considered for the planning and execution of observations apart from the overhead resulting from the reduced coronagraphic throughput of $\sim 59\%$, which should be taken into account in the exposure time calculations. The APP sits in the pupil plane and can be used in any of the common imaging modes (e.g., pupil tracking) once it is rotated in the light path.

5 sigma point source detection limit for VLT APP

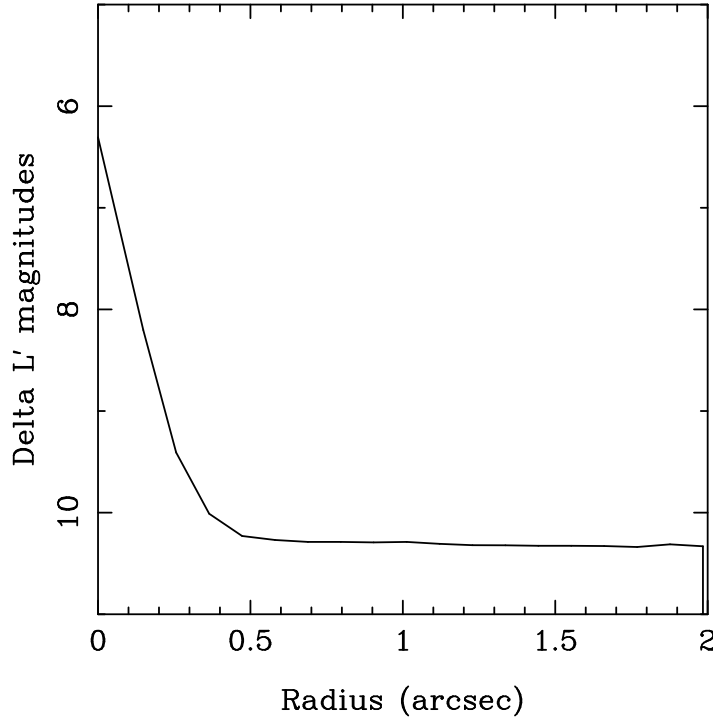


Figure 6. NACO/APP contrast curve for HIP61460 in the L' filter ($\lambda_{\text{cen}} = 3.8 \mu\text{m}$) and the observational setup described in Section 6.1.1. At $\sim 0.5''$ the sky background limit is reached.

Obviously one has to take into account, however, that only one hemisphere around a target shows an improved contrast behavior so that a second data set (with the FoV rotated by 180 deg) is required in order to cover both hemispheres around a target.

REFERENCES

1. Marois, C., Macintosh, B., Barman, T., Zuckerman, B., Song, I., Patience, J., Lafreniere, D., and Doyon, R., “Direct Imaging of Multiple Planets Orbiting the Star HR 8799,” *ArXiv e-prints* **322**, 1348– (Nov. 2008).
2. Kalas, P., Graham, J. R., Chiang, E., Fitzgerald, M. P., Clampin, M., Kite, E. S., Stapelfeldt, K., Marois, C., and Krist, J., “Optical Images of an Exosolar Planet 25 Light-Years From Earth,” *Science* **322**, 1–7 (Nov. 2008).
3. Lagrange, A.-M., Gratadour, D., Chauvin, G., Fusco, T., Ehrenreich, D., Mouillet, D., Rousset, G., Rouan, D., Allard, F., Gendron, É., Charton, J., Mugnier, L., Rabou, P., Montri, J., and Lacombe, F., “A probable giant planet imaged in the β Pictoris disk. VLT/NaCo deep L' -band imaging,” *A&A* **493**, L21–L25 (Jan. 2009).
4. Lagrange, A., Kasper, M., Boccaletti, A., Chauvin, G., Gratadour, D., Fusco, T., Ehrenreich, D., Apai, D., Mouillet, D., and Rouan, D., “Constraining the orbit of the possible companion to β Pictoris. New deep imaging observations,” *A&A* **506**, 927–934 (Nov. 2009).
5. Lafrenière, D., Jayawardhana, R., and van Kerkwijk, M. H., “The Directly Imaged Planet around the Young Solar Analog 1RXS J160929.1-210524: Confirmation of Common Proper Motion, Temperature and Mass,” *ArXiv e-prints* (June 2010).
6. Lagrange, A., Bonnefoy, M., Chauvin, G., Apai, D., Ehrenreich, D., Boccaletti, A., Gratadour, D., Rouan, D., Mouillet, D., Lacour, S., and Kasper, M., “A Giant Planet Imaged in the Disk of the Young Star β Pictoris. New deep imaging observations,” *Science* (June 2010).

7. Kenworthy, M. A., Codona, J. L., Hinz, P. M., Angel, J. R. P., Heinze, A., and Sivanandam, S., “First On-Sky High-Contrast Imaging with an Apodizing Phase Plate,” *ApJ* **660**, 762–769 (May 2007).
8. Stern, S. A., “The detectability of extrasolar terrestrial and giant planets during their luminous final accretion,” *AJ* **108**, 2312–2317 (Dec. 1994).
9. Mamajek, E. E. and Meyer, M. R., “An Improbable Solution to the Underluminosity of 2M1207B: A Hot Protoplanet Collision Afterglow,” *ApJL* **668**, L175–L178 (Oct. 2007).
10. Zahnle, K., Arndt, N., Cockell, C., Halliday, A., Nisbet, E., Selsis, F., and Sleep, N. H., “Emergence of a Habitable Planet,” *Space Science Reviews* **129**, 35–78 (Mar. 2007).
11. Miller-Ricci, E., Seager, S., and Sasselov, D., “The Atmospheric Signatures of Super-Earths: How to Distinguish Between Hydrogen-Rich and Hydrogen-Poor Atmospheres,” *ApJ* **690**, 1056–1067 (Jan. 2009).
12. Codona, J. L., Hinz, P. M., Kenworthy, M. A., Angel, J. R. P., and Woolf, N. J., “High-contrast phase apodization at the MMT: design and on-sky tests,” in [*Ground-based and Airborne Instrumentation for Astronomy*], McLean, I. S. and Iye, M., eds., *Proc. SPIE* **6269** (2006).
13. Codona, J., “Phase Apodization Coronagraphy,” in [*In the Spirit of Bernard Lyot: The Direct Detection of Planets and Circumstellar Disks in the 21st Century*], Kalas, P., ed., 24–+ (June 2007).